JOURNAL OF PROPULSION AND POWER
Vol. 18, No. 2, March–April 2002

Numerical Predictions of Channel Flows with Fluid Injection Using Reynolds-Stress Model

Bruno Chaouat*
ONERA, 92322 Châtillon, France

Numerical predictions of channel flows with fluid injection through a porous wall are performed by solving the time-dependent Navier–Stokes equations using a Reynolds-stress turbulent model. Influence of the turbulence injected fluid is investigated. Numerical results with experimental data indicate that the flows evolve significantly vs the distance from the front wall such that different regimes of flow development can be observed. In the first regime the velocity field is developed in accordance with the laminar theory. The second regime is characterized by the development of turbulence, which occurs at different locations in the channel because of the presence of impermeable and permeable walls, and by the transition process of the mean axial velocity when a critical turbulence threshold is attained. Computed results are compared with existing experimental data including axial mean velocity profiles and full turbulent stresses. As a result for the simulations, the Reynolds-stress model predicts the mean velocity profiles, the transition process, and the turbulent stresses, in good agreement with experimental data.

Nomenclature

A = flatness anisotropy parameter, $1 - \frac{9}{8}(A_2 - A_3)$
A_2 = second invariant, $a_{ij}a_{ji}$
A_3 = third invariant, $a_{ij}a_{jk}a_{ki}$
a_{ij} = Reynolds-stress anisotropy, $(\tau_{ij} - \frac{2}{3}k\delta_{ij})/k$
C_f = friction coefficient, $2(u_\tau/u_m)^2$
c_p = specific heat at constant pressure, J/(kg · K)
E = total specific energy, m²/s², J/kg
H = total specific enthalpy, $h + u_iu_i/2$, m²/s²
h = specific enthalpy, m²/s²
J_{ij} = tensor of diffusion for the Reynolds stress τ_{ij}
k = specific turbulent kinetic energy, $\tau_{ii}/2$, m²/s²
L = channel length, m
M = Mach number
m = injection mass flux, kg/(m² · s)
n_i = normal to the wall
P_{ij} = production rate of τ_{ij} caused by mean shear
P_{r_t} = turbulent Prandtl number
p = static pressure, Pa
q_i = total heat flux vector, W/m²
R_s = injection Reynolds number, $\rho_s u_s \delta/\mu_s$
R_t = turbulent Reynolds number $k^2/\nu\epsilon$
R_u = universal gas constant
S_{ij} = strain-rate tensor
s = specific entropy, J/(kg · K)
T = temperature, K
U = vector of conservative variables $\bar\rho$, $\bar\rho\tilde u_i$, $\bar\rho\tilde E$, $\bar\rho\widetilde{u_i''u_j''}$, $\bar\rho\epsilon$
u_i = velocity vector, m/s
u_m = bulk velocity, m/s
u_s = injection velocity, m/s
u_τ = friction velocity, m/s
x_i = Cartesian coordinate, m
x_i^+ = dimensionless distance from walls, x_iu_τ/ν
α = coefficient for planar or axisymmetric geometry
β = momentum flux coefficient,

$$\frac{\left(\rho\delta\int_0^\delta \bar\rho\tilde u_1^2\,\mathrm{d}x_2\right)}{\left(\int_0^\delta \bar\rho\tilde u_1\,\mathrm{d}x_2\right)^2}$$

γ = ratio of specific heats
δ = channel height, m
δ_{ij} = Kronecker tensor
ϵ = dissipation rate, m²/s³
ϵ_{ijk} = permutation tensor
κ = thermal conductivity, W/(m · K)
μ = dynamic viscosity, kg/(m · s)
ν = kinematic viscosity, m/s²
ρ = density, kg/m³
Σ_{ij} = total stress tensor
σ_{ij} = viscous stress tensor
σ_s = surface-generated pseudoturbulence, $(\widetilde{u_2''u_2''}/u_s^2)^{1/2}$
τ_{ij} = turbulent stress tensor, $\widetilde{u_i''u_j''}$
Φ_{ij} = pressure-strain fluctuations, $\overline{p'S_{ij}''}$
ω_i = vorticity tensor, $\epsilon_{ijk}\partial u_k/\partial x_j$, (1/s)

Subscripts

m = bulk mean quantity
s = condition at injection surface
w = wall

Superscripts

$\bar{}$ = Reynolds averaged of variable
$\tilde{}$ = Favre averaged of variable
$'$ = Reynolds turbulent fluctuating value of variable
$''$ = Favre turbulent fluctuating value of variable

Introduction

FLOWS through porous ducts with wall injection are encountered in many engineering applications such as transpiration cooling, boundary-layer control, and the combustion induced flowfield in solid-propellant rocket motors (SRM). For SRM applications[1] the flow plays an important role in ballistics prediction, which is affected by the transition behavior of the mean axial velocity and by turbulence quantities. The flow in the chamber of a solid rocket motor can be modeled by a duct flow with appreciable fluid injection through permeable walls. This type of flow evolves significantly with respect to the distance from the front wall. Different

Received 8 August 2000; revision received 13 September 2001; accepted for publication 1 October 2001.

*Senior Scientist, Computational Fluid Dynamics and Aeroacoustics Department. Member AIAA.

flow regimes can be observed depending on the injection Reynolds number $R_s = \rho_s u_s \delta/\mu_s$, defined with the injection density ρ_s, the velocity u_s, the dynamic viscosity μ_s at the porous surface, and with the radius of a cylindrical duct or the half-height of a planar channel δ. In the first regime the velocity field is developed in accordance with the laminar theory. The second flow regime is characterized by the development of turbulence and by the transition process of the mean axial velocity when a critical turbulence threshold is attained. For the first regime where the flow is mainly governed by the fluid injection, Taylor,[2] Culick,[3] and Yamada et al.[4] have analytically determined the velocity profiles

$$u_1 = u_s \frac{x_1}{\delta} \frac{\pi}{2^{1-\alpha}} \cos\left[\frac{\pi}{2}\left(\frac{x_2}{\delta}\right)^{\alpha+1}\right] \tag{1}$$

$$u_2 = -u_s \left(\frac{\delta}{x_2}\right)^{\alpha} \sin\left[\frac{\pi}{2}\left(\frac{x_2}{\delta}\right)^{\alpha+1}\right] \tag{2}$$

in a frame of reference where x_1 and x_2 are respectively the distances along the streamwise and normal directions and $\alpha = 0$ or 1 for planar or axisymmetric flows. Equation (1) shows that the axial velocity increases linearly with the axial distance and satisfies the no-slip condition of the Navier–Stokes equations because $u_1(\delta) = u_1(-\delta) = 0$. Because of the progress in computing power, channel flows with fluid injection through porous walls have been studied numerically by several authors. Varapaev and Yagodkin[5] and Casalis et al.[6] investigated the viscous stability of the flow in a channel. Relative to the stability of uninjected channel flow, their results showed that the neutral stability of the flow occured at a lower axial-flow Reynolds number for low values of injection Reynolds number and that the axial-flow Reynolds number at the neutral stability increased linearly for large values of injection Reynolds number. Sviridenkov and Yagodkin[7] assumed the flow to be incompressible and solved the time-average Navier–Stokes equations using k–ϵ and k–ω turbulence models. Their results provided different predictions of the transition process and overpredicted turbulence levels by about 300 and 200% in the posttransition of the flow. Beddini[8] solved a parabolic differential equations system using a turbulence model developed by Donalson.[9] This model is based on transport equations of the Reynolds stresses with an algebraic relation for the turbulence macro-length scale. The calculations overpredicted the experimental data of Yamada et al.[4] by about 200%, but a reasonable agreement with the data of Dunlap et al.[10] was obtained by generating pseudoturbulence at the porous surface. Sabnis et al.[11] applied the k–ϵ model for simulating the flowfield measured by Dunlap et al.[10] As for the previous simulations, the turbulence intensity was overpredicted by about 200%. Then, Sabnis et al.[12] attempted to predict the flowfield in the nozzleless solid rocket motor investigated experimentally by Traineau et al.[13] They empirically modified the damping functions of the k–ϵ model at low Reynolds number in order to obtain more accurate results. Chaouat[14] also investigated this flow[13] by means of k–ϵ turbulence model by setting the damping functions equal to unity yet discrepancies remained regarding the turbulence intensity. Liou and Lien[15] decided to solve the two-dimensional Navier–Stokes equations directly without turbulence model. Although the mesh resolution did not permit a direct numerical simulation of the internal flowfield, they indicated turbulence intensity profiles in good agreement with experimental data.[13] Recently, they have extended their previous simulation by solving the two-dimensional Navier–Stokes equations with a subgrid scale turbulence model.[16] The results of their simulations seem to demonstrate that large eddy structures play an important role in the flow. More recently, Apte and Yang[17] have solved the three-dimensional Navier–Stokes equations using a compressible version of a dynamic Smagorinsky model for simulating this flow.[13] The vortex-stretching and rolling mechanisms of the flow were well reproduced. As expected, these authors have mentioned that large eddy simulation must be three-dimensional for predicting fairly well the Reynolds stress intensity.

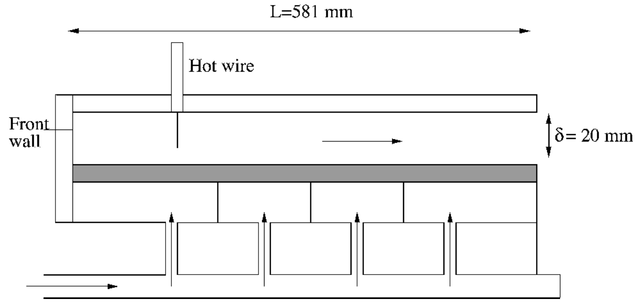

Fig. 1 Schematic of VECLA facility.

A recent specific experimental setup has been realized at ONERA for investigating the characterictics of injection driven flows. The experimental setup is sketched in Fig. 1. The planar experimental facility is composed of a parallelepiped channel bounded by a porous plate and impermeable walls. The value of the duct length is $L = 58.1$ cm. The channel height is 1.03 cm, and the width is 6 cm. Cold air at 303 K is injected with a uniform mass flow rate $m = 2.619$ kg/m^{2}s through porous material of porosities, 8 or 18 μm. The injection velocities are fixed by the local pressure in the channel. The pressure at the head end of the channel is 1.5 bar. In the exit section the pressure is 1.374 bar in accordance with the operating of the experimental setup. From the definition of the injection Reynolds number already mentioned, δ corresponds to the height of the channel caused by the nonsymmetry of the setup. Taking into account these parameters, the value of the injection Reynolds number is approximately 1600. Because of the mass conservation, the flow Reynolds number $R_m = \rho_m u_m \delta/\mu_m$ based on the bulk density ρ_m and the bulk velocity u_m varies linearly vs the axial distance of the channel. It ranges from zero to approximately the value 9×10^4. Experiments in three-dimensional geometry have been carried out at ONERA by Avalon et al.[18] The mean velocity profiles and the Reynolds-stress turbulent intensities have been measured with a hot-wire probe in eight sections of the channel located at $x_1 = 3.1$, 12, 22, 35, 40, 45, 50, and 57 cm. The hot-wire probe is introduced in the channel through the impermeable wall, as indicated in Fig. 1.

The objective of the present study is to investigate the flow in the experimental facility VECLA.[18] In this aim numerical flowfield predictions are performed by solving the time-averaged Navier–Stokes equations of mass, momentum, and energy using a Reynolds-stress model (RSM). This model is based on the transport equations of each individual component of the Reynolds-stress tensor and the transport equation of the dissipation rate. The use of such a turbulent model is motivated by the fact that it represents a good compromise between large eddy simulations that require very large computing time and first-order models that fail to predict complex flows accurately, as for instance, flows with strong effects of streamline curvature. Contrary to first-order turbulence models, second-order turbulence models are based on the pressure-strain correlation term,[19] which plays a pivotal role in determining the structure of turbulent flows. This term of major importance redistributes turbulent energy among the Reynolds-stress components. For calculations of complex wall-bounded turbulent flows, a wall reflection term[20] is generally incorporated in that model to account for the surface contribution from the solution of the Poisson equation. In a more practical approach some statistical models[21–23] (V2F type model) have been developed recently, which are a simplified version of RSM models. These require only the transport equations of the turbulent kinetic energy, the correlation of the normal fluctuating velocities, and the dissipation rate. In that formulation an elliptic equation is introduced and interpreted as an approximation of the wall effects.

The RSM model used in this application has been originally developed by Launder and Shima.[24] This model is selected because its formulation is simpler and requires less empirical adjustments than most other models. Therefore, it is a good candidate to handle a large variety of flows. In the present study this model has been extended for compressible flows in a similar way of Huang and Coakley[25] and modified for simulating injection induced flows. It has accurately predicted rotating channel flows.[26]

Governing Equations

Turbulent flow of a viscous fluid is considered. As in the usual treatments of turbulence, the flow variable ξ is decomposed into ensemble Reynolds mean and fluctuating parts as follows:

$$\xi = \bar{\xi} + \xi' \tag{3}$$

In the present case the Favre average is used[27] for a compressible fluid so that the variable ξ can be written as

$$\xi = \tilde{\xi} + \xi'' \tag{4}$$

with the particular properties $\tilde{\xi}'' = 0$ and $\overline{\rho\xi''} = 0$. These relations imply that $\tilde{\xi} = \overline{\rho\xi}/\bar{\rho}$. The Reynolds average of the Navier–Stokes equations produces in Favre variables the following forms of the mass, momentum, and energy equations[28]:

$$\frac{\partial\bar{\rho}}{\partial t} + \frac{\partial}{\partial x_j}(\bar{\rho}\tilde{u}_j) = 0 \tag{5}$$

$$\frac{\partial}{\partial t}(\bar{\rho}\tilde{u}_i) + \frac{\partial}{\partial x_j}(\bar{\rho}\tilde{u}_i\tilde{u}_j) = \frac{\partial\bar{\Sigma}_{ij}}{\partial x_j} \tag{6}$$

$$\frac{\partial}{\partial t}(\bar{\rho}\tilde{E}) + \frac{\partial}{\partial x_j}(\bar{\rho}\tilde{E}\tilde{u}_j) = \frac{\partial}{\partial x_j}\left(\bar{\Sigma}_{ij}\tilde{u}_i\right) + \frac{\partial}{\partial x_j}\left(\overline{\sigma_{ij}u_i''} - \frac{1}{2}\bar{\rho}\widetilde{u_k''u_k''u_j''}\right) - \frac{\partial\bar{q}_j}{\partial x_j} \tag{7}$$

The mean stress tensor $\bar{\Sigma}_{ij}$ is composed by the mean pressure $\bar{p}$, the mean viscous stress $\bar{\sigma}_{ij}$, and the turbulent stress $\bar{\rho}\,\tau_{ij}$ as follows:

$$\bar{\Sigma}_{ij} = -\bar{p}\delta_{ij} + \bar{\sigma}_{ij} - \bar{\rho}\tau_{ij} \tag{8}$$

In this expression the tensor $\bar{\sigma}_{ij}$ takes the usual form:

$$\bar{\sigma}_{ij} = 2\bar{\mu}\bar{S}_{ij} - \frac{2}{3}\bar{\mu}\frac{\partial\bar{u}_k}{\partial x_k}\delta_{ij} \tag{9}$$

where the mean strain rate $\bar{S}_{ij}$ and and the Favre-averaged Reynolds-stress tensor τ_{ij} are defined respectively by

$$\bar{S}_{ij} = \frac{1}{2}\left(\frac{\partial\bar{u}_i}{\partial x_j} + \frac{\partial\bar{u}_j}{\partial x_i}\right) \tag{10}$$

$$\tau_{ij} = \widetilde{u_i''u_j''} \tag{11}$$

and μ is the molecular viscosity. Assuming ideal-gas law, the mean thermodynamic pressure is computed by

$$\bar{p} = (\gamma - 1)\bar{\rho}\left(\tilde{E} - \tfrac{1}{2}\tilde{u}_i\tilde{u}_i - \tfrac{1}{2}\tau_{ii}\right) \tag{12}$$

The presence of the turbulent contribution τ_{ii} in Eq. (12) shows a coupling between the mean equations and the turbulent transport equations. The mean heat flux $\bar{q}_i$ is composed by the laminar and turbulent flux contributions:

$$\bar{q}_i = -\bar{\kappa}\frac{\partial\bar{T}}{\partial x_i} + \bar{\rho}\,\widetilde{h''u_i''} \tag{13}$$

Closure of the mean flow equations is necessary for the turbulent stress $\bar{\rho}\,\widetilde{u_i''u_j''}$, the molecular diffusion $\overline{\sigma_{ij}u_i''}$, the turbulent transport of the turbulent kinetic energy $\bar{\rho}\,\widetilde{u_k''u_k''u_j''}$, and the turbulent heat flux $\bar{\rho}\,\widetilde{h''u_i''}$.

Turbulence Model

The Favre-averaged correlation tensor $\tau_{ij} = \widetilde{u_i''u_j''}$ is computed by means of a transport equation as follows:

$$\frac{\partial}{\partial t}(\bar{\rho}\tau_{ij}) + \frac{\partial}{\partial x_k}(\bar{\rho}\tau_{ij}\tilde{u}_k) = P_{ij} - \frac{2}{3}\bar{\rho}\epsilon\delta_{ij} + \Phi_{(1)ij} + \Phi_{(2)ij} + \Phi_{(w)ij} + J_{ij} \tag{14}$$

where

$$P_{ij} = -\bar{\rho}\tau_{ik}\frac{\partial\tilde{u}_j}{\partial x_k} - \bar{\rho}\tau_{jk}\frac{\partial\tilde{u}_i}{\partial x_k} \tag{15}$$

$$\Phi_{(1)ij} = -c_1\bar{\rho}\epsilon a_{ij} \tag{16}$$

$$\Phi_{(2)ij} = -c_2\left(P_{ij} - \frac{1}{3}P_{kk}\delta_{ij}\right) \tag{17}$$

$$\Phi_{(w)ij} = c_{w1}\frac{\bar{\rho}\epsilon}{k}\left(\tau_{kl}n_kn_l\delta_{ij} - \frac{3}{2}\tau_{ki}n_kn_j - \frac{3}{2}\tau_{kj}n_kn_i\right)f_w + c_{w2}\left(\Phi_{(2)kl}n_kn_l\delta_{ij} - \frac{3}{2}\Phi_{(2)ik}n_kn_j - \frac{3}{2}\Phi_{(2)jk}n_kn_i\right)f_w \tag{18}$$

$$J_{ij} = \frac{\partial}{\partial x_k}\left(\bar{\mu}\frac{\partial\tau_{ij}}{\partial x_k} + c_s\bar{\rho}\frac{k}{\epsilon}\tau_{kl}\frac{\partial\tau_{ij}}{\partial x_l}\right) \tag{19}$$

The terms on the right-hand side of Eq. (14) are identified as production by the mean flow, dissipation rate, slow redistribution, rapid redistribution, wall reflection and diffusion. In these expressions $k = \tau_{ii}/2$ is the turbulent kinetic energy, and $a_{ij} = (\tau_{ij} - \frac{2}{3}k\delta_{ij})/k$ is the anisotropic tensor. The functions c_1, c_2, c_{w1}, c_{w2} depend on the second and third invariants $A_2 = a_{ij}a_{ji}$, $A_3 = a_{ij}a_{jk}a_{ki}$, the flatness coefficient parameter $A = 1 - \frac{9}{8}(A_2 - A_3)$, and the turbulent Reynolds number $R_t = k^2/\nu\epsilon$. The dissipation rate ϵ in expression (14) is computed by means of the following transport equation:

$$\frac{\partial}{\partial t}(\bar{\rho}\epsilon) + \frac{\partial}{\partial x_j}(\bar{\rho}\tilde{u}_j\epsilon) = \frac{\partial}{\partial x_j}\left(\bar{\mu}\frac{\partial\epsilon}{\partial x_j} + c_\epsilon\bar{\rho}\frac{k}{\epsilon}\tau_{jl}\frac{\partial\epsilon}{\partial x_l}\right) - (c_{\epsilon1} + \psi_1 + \psi_2)\bar{\rho}\frac{\epsilon}{k}\tau_{ij}\frac{\partial\tilde{u}_j}{\partial x_i} - c_{\epsilon2}\bar{\rho}\frac{\tilde{\epsilon}\epsilon}{k} \tag{20}$$

where

$$\tilde{\epsilon} = \epsilon - 2\nu\left(\frac{\partial\sqrt{k}}{\partial x_2}\right)^2 \tag{21}$$

Values of the constant coefficients are $c_s = 0.22$, $c_{\epsilon1} = 1.45$, $c_{\epsilon2} = 1.9$, $c_\epsilon = 0.18$. The functions suggested by Shima[29] are listed in Table 1. Relative to the original model, the function ψ_1 has been modified for simulating injection induced flows that are far from equilibrium state because its value can be too large in comparison with the standard value $c_{\epsilon1}$. Therefore, ψ_1 has been bounded, $|\psi_1| < 0.125\,c_{\epsilon1}$. This has the effect of preventing to early laminarization of the flows. On the other hand, the function ψ_2 has been set to zero because of its empirical foundation.

Table 1 Functions in the model of Shima

Functions	Expressions
c_1	$1 + 2.58AA_2^{1/4}\{1 - \exp[-(0.0067R_t)^2]\}$
c_2	$0.75A^{1/2}$
c_{w1}	$-\frac{2}{3}c_1 + 1.67$
c_{2w}	$\max(\frac{2}{3}c_2 - \frac{1}{6}, 0)/c_2$
f_w	$0.4k^{3/2}/\epsilon x_2$
ψ_1	$1.5A(P_{ii}/2\bar{\rho}\epsilon - 1)$
ψ_2	$0.35(1 - 0.3A_2)\exp[-(0.002R_t)^{1/2}]$

Regarding the molecular diffusion and the turbulent transport terms, a gradient hypothesis has been proposed:

$$\overline{\sigma_{ij}u_i''} - \frac{1}{2}\bar{\rho}\widetilde{u_k''u_k''u_j''} = \left(\bar{\mu}\delta_{jm} + c_s\bar{\rho}\frac{k}{\epsilon}\tau_{jm}\right)\frac{\partial k}{\partial x_m} \tag{22}$$

For the heat transfer the turbulent flux is computed by means of the k and ϵ variables:

$$\widetilde{h''u_i''} = -\frac{c_\mu k^2}{\epsilon}\frac{c_p}{P_{r_t}}\frac{\partial \bar{T}}{\partial x_i} \tag{23}$$

The coefficient c_μ takes the standard value of 0.09.

Numerical Approach

Numerical Algorithm

The computations have been performed in two-dimensional geometry. This is a good approximation because the experimental setup is relatively wide (width of 6 cm, height of 1.03 cm) such that the geometric shape factor is approximately six. The finite volume technique is adopted in the present code[30] to solve the full transport equations. The vector of the unknown variables is formed by the mass density, the momentum, the total energy, the Reynolds stresses, and the dissipation rate as indicated by

$$U^T = (\bar{\rho}, \bar{\rho}\tilde{u}_1, \bar{\rho}\tilde{u}_2, \bar{\rho}\tilde{E}, \bar{\rho}\widetilde{u_1''u_1''}, \bar{\rho}\widetilde{u_1''u_2''}, \bar{\rho}\widetilde{u_1''u_3''}, \bar{\rho}\widetilde{u_2''u_2''}, \bar{\rho}\widetilde{u_2''u_3''}, \bar{\rho}\widetilde{u_3''u_3''}, \bar{\rho}\epsilon) \tag{24}$$

For the two-dimensional computations it is assumed that the mean velocity and the mean gradients are zero in the spanwise direction x_3. As expected in that condition, the RSM model produces turbulent quantities $\widetilde{u_1''u_3''}$ and $\widetilde{u_2''u_3''}$ equal to zero. The correlation $\widetilde{u_3''u_3''}$ is computed by the slow part of the redistribution term $\Phi_{(1)33}$ and by the diffusive term J_{33}. But this component $\tau_{33} = \widetilde{u_3''u_3''}$ does not affect the mean motion, as indicated by Eq. (6). The vector U is calculated at the center of each cell, whereas the fluxes F at the cell interfaces are computed by means of an approximate Riemann solvers as follows:

$$F = [F(U_R) + F(U_L)]/2 - |B|[(U_R - U_L)/2] \tag{25}$$

where $|B|$ is the absolute Jacobian matrix computed at the interface by the Roe average.[31] The two approximations U_R and U_L for the left and right sides are evaluated on each interface of the mesh using a MUSCL approach.[32] The numerical scheme is second-order accurate in space discretization. The governing equations are integrated explicitely in time using a three-step Runge–Kutta method. No artificial dissipation is added in the numerical scheme in order to not alter the solving of the transport equations. The code has been previously calibrated with the case of fully developed turbulent channel flows.[30] In the present computations a local time-step technique is used to accelerate convergence to the stationary state. For each simulation convergence of the numerical results is achieved when the average residual profiles go to zero for each dependant variable. In this case it is also verified that the ratio of exit mass flow to the injected mass flow is close to unity (within 0.1%).

Boundary and Initial Conditions

Different boundary conditions are applied in the computational domain shown in Fig. 2. For the impermeable walls no slip on velocity and constant temperature $\bar{T}_w$ are required. The turbulent kinetic energy $k_w = 0$ and the wall dissipation rate value $\epsilon_w = 2\nu(\partial\sqrt{k}/\partial x_2)^2$, are specified.[33] The reflection of the pressure-strain fluctuations from the rigid wall are taken into account through the term $\Phi_{(w)ij}$ in the transport equation of the Reynolds-stress tensor (14). For the permeable wall the inflow boundary condition requires a constant mass flow rate at the same temperature T_w. This implies that the mean injection velocity u_s along the normal direction to the wall is computed as

$$u_s = c_p\left[-\bar{p}/mR_u + \sqrt{[(\bar{p}/mR_u)]^2 + 2\bar{T}_w/c_p}\right] \tag{26}$$

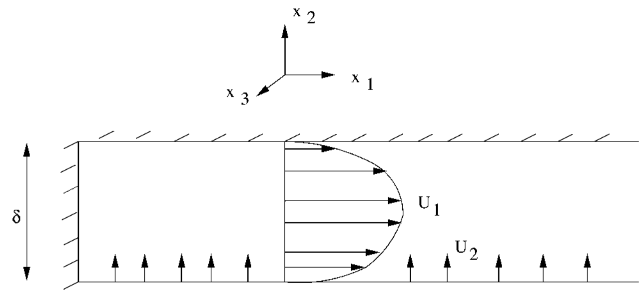

Fig. 2 Schematic of channel flow with fluid injection.

The turbulent boundary conditions applied at the porous wall are an important issue of the present work. Experimental investigations[34–36] of injected air from porous plates indicate that some stationary velocity fluctuations appear in the flow and that disturbance amplitude increases with increasing injection velocity. Recently, regarding the VECLA facility, Avalon et al.[18] have also shown that the pseudoturbulence intensity close to the porous wall depends on the porosity and the injection velocity. Consequently, the turbulence fluctuations at the porous surface can be related to the mean injection velocity by means of a coefficient defined as $\sigma_s = (\widetilde{u_2''u_2''}/u_s^2)^{1/2}$ to be parametrically investigated. Other correlations such as $\widetilde{u_1''u_1''}$ or $\widetilde{u_3''u_3''}$ are smaller than the normal velocity fluctuations $\widetilde{u_2''u_2''}$ of the injected flow. In this work several simulations are performed for investigating the influence of turbulence in injected fluid for the values $\sigma_s = 0.1$, 0.2, 0.3, 0.4, and 0.5. For injection of velocities of low intensity, the standard value of the wall dissipation rate ϵ_w is imposed at the porous surface. This assumes that the porosity of the porous plate is fine grained (8 μm). Another point to emphazise concerns the pressure fluctuations. Considering that the permeable wall does not reflect the pressure fluctuations, the term $\Phi(w)ij$ of Eq. (14) is reduced to zero in the normal direction to the permeable wall. A pressure boundary condition is applied for the exit section of the channel.

Grid Independance

Numerical simulations are performed on refined meshes requiring 100×100, 200×200, and 200×300 nonuniform grids in x_1 and x_2 directions. For all of the meshes, the grid in the normal direction x_2 is distributed using two geometric progressions from the wall to the center of the channel. For instance, the transverse resolution for the mesh 100×100 is 1 μm near the walls and 200 μm in the center of the channel. From zero to 0.5 mm, there are 20 points distributed with a geometric progression of 1.128. From 0.5 to 5.1 mm, 30 points are distributed with a geometric progression of 1.022. The dimensionless distance $x_2^+ = x_2 u_\tau/\nu$ between the first node and the wall is less than 0.3. In such conditions this grid refinement provides full resolutions for the flow in the permeable wall region and for the boundary layer generated by the rigid walls. A grid-independence study was performed by checking the axial mean velocity and the turbulence intensity. In the case where the grid resolution along the normal direction is not refined, it has been observed that the distribution of the turbulence intensity of the channel flow is slightly modified. The turbulence is less developed in the wall region. Computations have shown in this case that the turbulent kinetic energy and the dissipation rate levels are influenced by the boundary condition of the dissipation rate at the wall. As known, the dissipation rate presents a very strong variation in the wall region. It must be computed accurately. The flow predictions appear less sensitive to the mesh refinement in the streamwise direction x_1.

Numerical Results

Streamlines and Mean Flow Contours

The streamlines and the mean flow contours are presented for the simulation performed with the injection parameter $\sigma_s = 0.2$. Figure 3 shows the streamlines and the mean velocities of the flowfield. Strong effects of the streamlines curvature are observed near

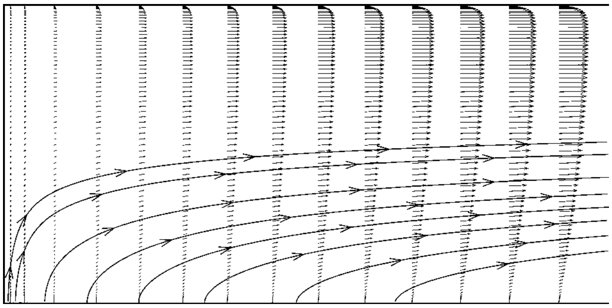

Fig. 3 Streamlines and mean flow velocity field: $\sigma_s = 0.2$.

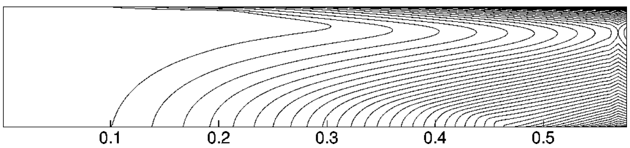

Fig. 4 Mean dimensionless entropy contours; $11.15 < s/c_v < 11.19$; $\Delta = 0.001$; $\sigma_s = 0.2$.

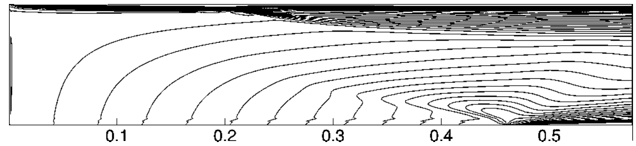

Fig. 5 Mean vorticity contours; $-5.10^3 < \tilde{\omega}_3 < 10^5$; $\Delta = 1000$ (1/s); $\sigma_s = 0.2$.

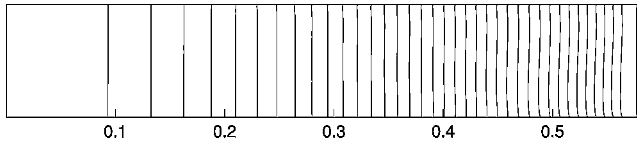

Fig. 6 Mean pressure contours; $1.37 < p < 1.53$; $\Delta = 0.004$ bar; $\sigma_s = 0.2$.

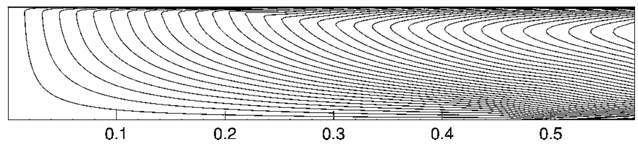

Fig. 7 Mach-number contours; $0 < \text{Mach} < 0.35$; $\Delta = 0.01$; $\sigma_s = 0.2$.

the porous wall as a result of the fluid injection. The velocities increase rapidly in the boundary layer generated by the rigid wall. Figure 4 represents the mean dimensionless entropy contours $\bar{s}/c_v$ of the flowfield. It is shown that the trajectories of the entropy lines depart from the permeable wall and move to the exit section of the channel. Applicable to the analysis of the variation of entropy are Crocco's equation for steady viscous flows and the steady-state energy equation given respectively by

$$T\frac{\partial s}{\partial x_i} = \epsilon_{ijk}\,\omega_j u_k + \frac{\partial H}{\partial x_i} - \frac{1}{\rho}\frac{\partial \sigma_{ij}}{\partial x_i} \tag{27}$$

$$u_j\frac{\partial H}{\partial x_j} = \frac{1}{\rho}\frac{\partial}{\partial x_j}(\sigma_{ij}u_i) - \frac{H}{\rho}\frac{\partial}{\partial x_j}(\rho u_j) \tag{28}$$

where $\omega_i = \epsilon_{ijk}\partial u_k/\partial x_j$ is the vorticity tensor. In the region of the channel where viscous diffusion, turbulence, and compressible effects can be neglected, Eq. (28) shows that the total enthalpy is constant along the streamlines of the flow. Because the injection boundary condition is applied at the permeable wall, the stagnation enthalpy has approximately the same constant value along all of the streamlines. Therefore, the enthalpy gradient of Eq. (27) vanishes. Considering that the temperature is almost uniform in the channel and taking into account the vorticity term $\epsilon_{ijk}\omega_j u_k$ as well as the velocity profile (1) for a planar symmetric channel, resolution of Eq. (27) yields the expression for the entropy

$$s = \frac{\pi^2 u_s^2 x_1^2}{8\delta^2 T}\sin^2\left(\frac{\pi x_2}{2\delta}\right) \tag{29}$$

For the VECLA configuration the value at the permeable wall is $s_s = \pi^2 u_s^2 x_1^2/8\delta^2 T$. This relation shows that the entropy is dependent of the injection velocity u_s at the wall. Moreover, it varies as a quadratic function of the axial distance along the channel, as shown by the distribution of the entropy contours. The entropy profile (29) satisfies the steady convective equation $u_j\,\partial s/\partial x_j = 0$. In the case of a turbulent flow regime, the entropy is also created by the turbulent correlation $\overline{\omega_j' u_k'}$. Figure 5 shows the mean vorticity contours in the channel. It can be seen that the magnitude of the vorticity increases rapidly at two locations; one near the impermeable wall ($x_1 = 0.20$ m) and the other near the permeable wall ($x_1 = 0.48$ m), corresponding to the flow transition. The oscillations of the curves, which appear near the permeable wall, correspond to the physical instabilities of the shear stress, which are produced by the fluid injection. The evolution of the mean vorticity can be explained by its transport equation (30) in a steady flow regime:

$$\tilde{u}_j\frac{\partial \tilde{\omega}_i}{\partial x_j} = \nu\frac{\partial^2 \tilde{\omega}_i}{\partial x_j \partial x_j} - \frac{\partial}{\partial x_j}\left(\overline{\omega_i'' u_j''}\right) + \tilde{\omega}_j\tilde{S}_{ij} + \overline{\omega_j'' S_{ij}''} + O \tag{30}$$

where O represents the term of compressible flow effects, which can be neglected. For a two-dimensional computation the mean vorticity is along the spanwise direction $\tilde{\omega}_3 = (\partial\tilde{u}_2/\partial x_1 - \partial\tilde{u}_1/\partial x_2)$. It is created by the interaction between the flow injected in the normal direction to the permeable wall and the flow coming from the head end of the channel in the streamwise direction. The vorticity is convected by the main flow velocity and modified by the laminar and turbulent diffusion processes as indicated by Eq. (30). The gain or loss of the mean vorticity is only caused by the correlation term $\overline{\omega_j'' S_{ij}''}$ composed of the fluctuating vorticity components and by fluctuating strain rates. The laminar contribution $\tilde{\omega}_j\tilde{S}_{ij}$ is reduced to zero for two-dimensional mean flow. Figure 6 shows the mean pressure contours of the channel flow and reveals that the pressure is uniform in each cross section of the channel. Figure 7 illustrates the Mach-number contours of the channel flow. High resolution of the steady-state computational flowfield can be observed through the regular behavior of the contour lines. The Mach-number ranges from zero in the head end of the channel to approximately 0.35 in the exit section of the channel.

Effect of Turbulence in Injected Fluid

Several simulations have been performed to investigate the influence of the turbulence injection by means of the parameter coefficient σ_s. As it could be expected, the turbulence transition is affected by the pseudoturbulence injected through the porous wall. Figure 8 shows the contours of the turbulent kinetic energy for the simulations performed with the injection parameter $\sigma_s = 0.1$, 0.2, 0.3, 0.4, and 0.5. Because of the presence of permeable and impermeable walls, the development of the turbulence occurs at two different locations in the channel. In particular, it can be seen that the turbulence is developed more rapidly near the impermeable wall region. Relative to the stability of channel flow bounded by impermeable walls, this result is in agreement with the fact that the stability of channel flow with fluid injection through the walls increases with the injection Reynolds number, as shown in Fig. 9. This is attributed to the effects of favorable pressure gradient in the permeable wall region, as mentioned by Varapaev and Yagodkin.[5] Figure 8 also indicates that increasing the pseudoturbulence intensity has the effect of triggering early the transition process near the permeable wall. This

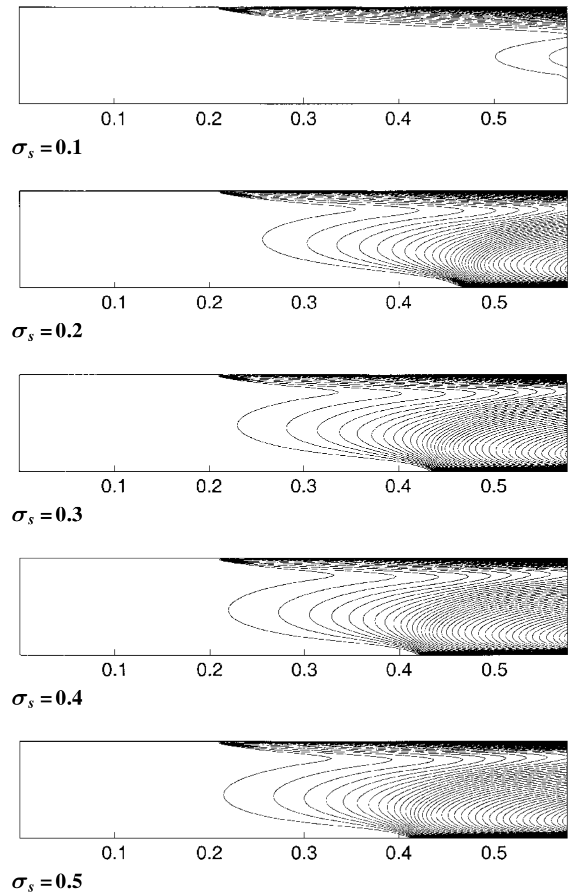

Fig. 8 Contours of turbulent kinetic energy; $0 < k < 160$; $\Delta = 5\ \mathrm{m^2/s^2}$.

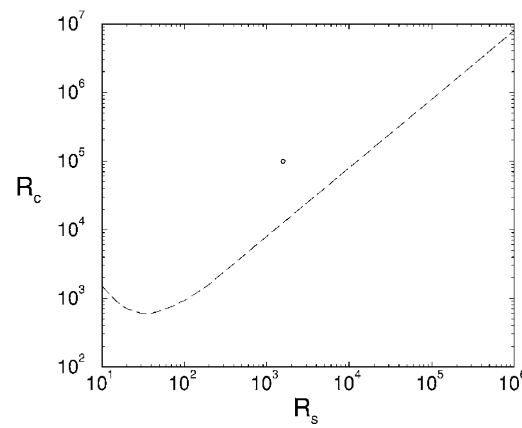

Fig. 9 Variation of axial-flow Reynolds number $R_c = \rho_c u_c \delta/\mu$ for stability vs the injection Reynolds number $R_s = \rho_s u_s \delta/\mu$: - - -, linear stability analysis[5]; and ○, present computation.

signifies that fluid injection with high turbulence intensity destabilizes the channel flow more rapidly than a fluid injection with low turbulence intensity. As a consequence, the transition location near the permeable wall shifts in the upstream direction. On the other hand, the transition of the turbulence near the impermeable wall remains unaffected by turbulence in injected fluid. Figure 8 shows that the contour lines of the turbulent kinetic energy have a similar evolution at the downstream location of the mean flow transition for $\sigma_s = 0.2$, 0.3, 0.4, and 0.5. In the case of a low turbulence level computed with $\sigma_s = 0.1$, a different distribution of the turbulence is observed in the channel. This is also illustrated in Fig. 10, which shows for different values of the injection parameter the evolution of the integral momentum flux coefficient[37] defined by

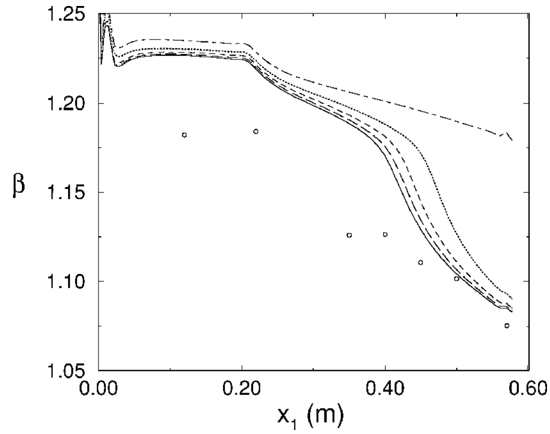

Fig. 10 Axial variations of the coefficient β: ○, experimental data; –·–, $\sigma_s = 0.1$; · · · · ·, $\sigma_s = 0.2$; - - - -, $\sigma_s = 0.3$; – – –, $\sigma_s = 0.4$; and ——, $\sigma_s = 0.5$.

$$\beta = \frac{\bar{\rho}\delta \int_0^\delta \bar{\rho}\tilde{u}_1^2 \,\mathrm{d}x_2}{\left(\int_0^\delta \bar{\rho}\tilde{u}_1 \,\mathrm{d}x_2\right)^2} \tag{31}$$

Effects of the pseudoturbulence injected at the porous wall is well described in this figure. The rapid drops of the coefficient β correspond to the transition locations of the mean velocity profiles, which occur near the impermeable wall region and afterward near the permeable wall region. It can be noticed that the low initial turbulence injection at the permeable wall for $\sigma_s = 0.1$ is too small to trigger the second transition process near the permeable wall region. This figure reveals a qualitative agreement with the experimental data, but a discrepancy in the magnitude remains in the laminar region of the flow. It is of interest to compute the coefficient β analytically using the laminar velocity profile. The profile of Eq. (1) can be extended to the VECLA configuration in the range domain $[0, \delta]$ with $u_1(0) = 0$ although the effects of the laminar boundary layer for $x_2 = \delta$ are not taken into account in this relationship:

$$u_1 = u_s \frac{x_1}{\delta} \frac{\pi}{2} \cos\left[\frac{\pi(\delta - x_2)}{2\delta}\right] \tag{32}$$

Computation of the coefficient β taking into account integration of the profile (32) over the domain $[0, \delta]$ yields the value $\pi^2/8 \approx 1.23$, which is quite close to the numerical value predicted by the simulations. This value corresponds strickly to a symmetrical flow with two-wall injection with respect to the centerline. In the VECLA setup the effect of the nonsymmetry flow on the β value becomes more and more negligible for the laminar flow regime as the axial distance from the head end increases. In this case β goes to 1.23. This approximation is not valid very close the head end where the Mach number goes to zero. This phenomena explains the oscillation values of β in that region. A more definitive way to determine the axial location of the mean flow transition consists in examining the local variation of the skin-friction coefficient C_f defined as

$$C_f = 2(u_\tau/u_m)^2 \tag{33}$$

where the bulk velocity u_m is computed by integration over the channel height:

$$u_m = \frac{1}{\delta} \int_0^\delta \bar{u}_1 \,\mathrm{d}x_2 \tag{34}$$

and where the friction velocity u_τ is computed on the permeable wall $u_{\tau s} = u_\tau(0)$ or on the impermeable wall $u_{\tau w} = u_\tau(\delta)$. Figure 11 shows the evolution of the skin-friction coefficient computed for the impermeable and permeable walls. As can be observed, the rapid increases of this coefficient reveal the transition locations of the mean-velocity profile, which occurs at different stations in the channel.

Table 2 Mean flow variables

x_1, cm	u_s, m/s	u_m, m/s	u_{τ_s}, m/s	u_{τ_w}, m/s
3.1	1.48	4.62	0.11	0.65
12.0	1.49	17.24	0.20	1.23
22.0	1.50	32.18	0.29	2.67
35.0	1.54	52.44	0.38	4.19
40.0	1.56	60.09	0.41	4.74
45.0	1.58	68.30	0.42	5.15
50.0	1.60	77.07	1.02	5.63
57.0	1.65	89.27	1.65	6.32

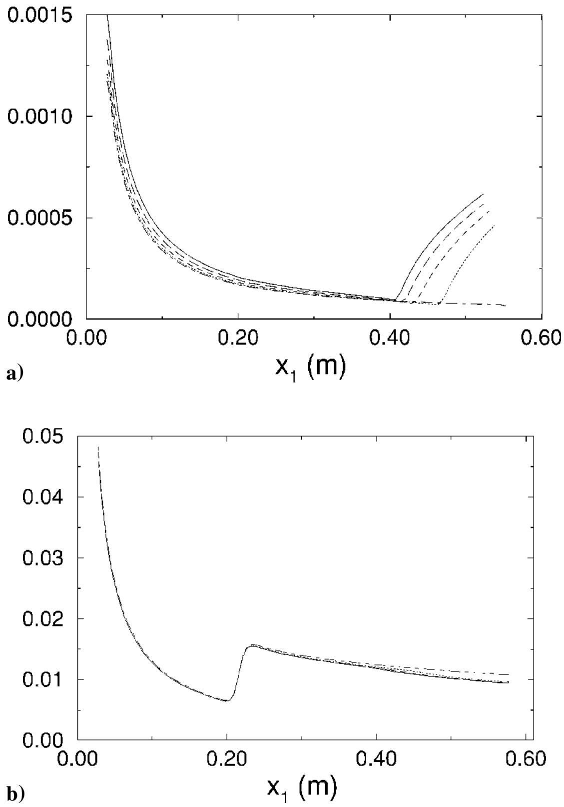

Fig. 11 Axial variation of the skin coefficient c_f: a) permeable wall; b) impermeable wall: –·–, $\sigma_s = 0.1$; · · · · ·, $\sigma_s = 0.2$; - - - -, $\sigma_s = 0.3$; – – –, $\sigma_s = 0.4$; and ——, $\sigma_s = 0.5$.

Mean Velocity and Turbulent Profiles

Table 2 indicates the mean flow variables at different stations of the channel. Figure 12 shows the dimensionless mean velocity profiles $\bar{u}_1/u_s$ in global coordinates x_2/δ in different cross sections of the channel for the RSM prediction performed with $\sigma_s = 0.2$. For the first sections in the channel, the laminar velocity profiles computed without turbulence modeling are also represented as dotted lines in this figure. Relative to the permeable wall region, it can be noticed that the velocities in the boundary layer generated by the impermeable wall increases rapidly. This figure shows that the general shapes of the RSM profiles present good agreement with experimental data although a minor difference persists for the velocity profiles computed in the sections located at 40 and 45 cm. The laminar velocity profiles also follow very well the experimental data at the stations $x_1 = 3.1$, 12, and 22 cm, but large discrepancies caused by the turbulence effects of the flow are shown for the laminar profile computed at the station $x_1 = 40$ cm. As already observed in the preceding figures, the first transition of the mean velocity occurs in the channel at the station $x_1 = 20$ cm.

Figure 13 shows the evolutions of the streamwise, normal, and cross turbulent velocity fluctuations normalized by the bulk velocity, $(\widetilde{u_1''u_1''})^{1/2}/u_m$, $(\widetilde{u_2''u_2''})^{1/2}/u_m$, $(\widetilde{u_1''u_2''})/u_m^2$, in different sections of the channel located at $x_1 = 22$, 35, 45, and 57 cm. The levels of

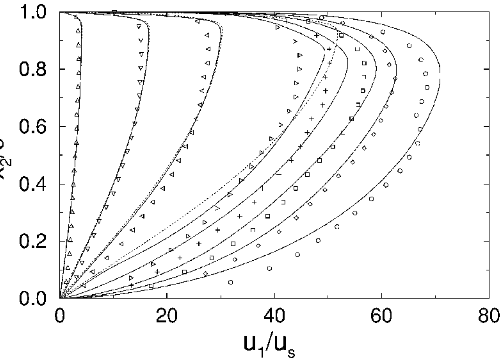

Fig. 12 Mean dimensionless velocity profiles in different sections: $\sigma_s = 0.2$. Symbols, experimental data; · · · · ·, laminar profiles; ——, RSM. $x_1 = 3.1$ cm: △; 12 cm: ▽; 22 cm: ◁; 35 cm: ▷; 40 cm: +; 45 cm: □; 50 cm: ◊; 57 cm: ○.

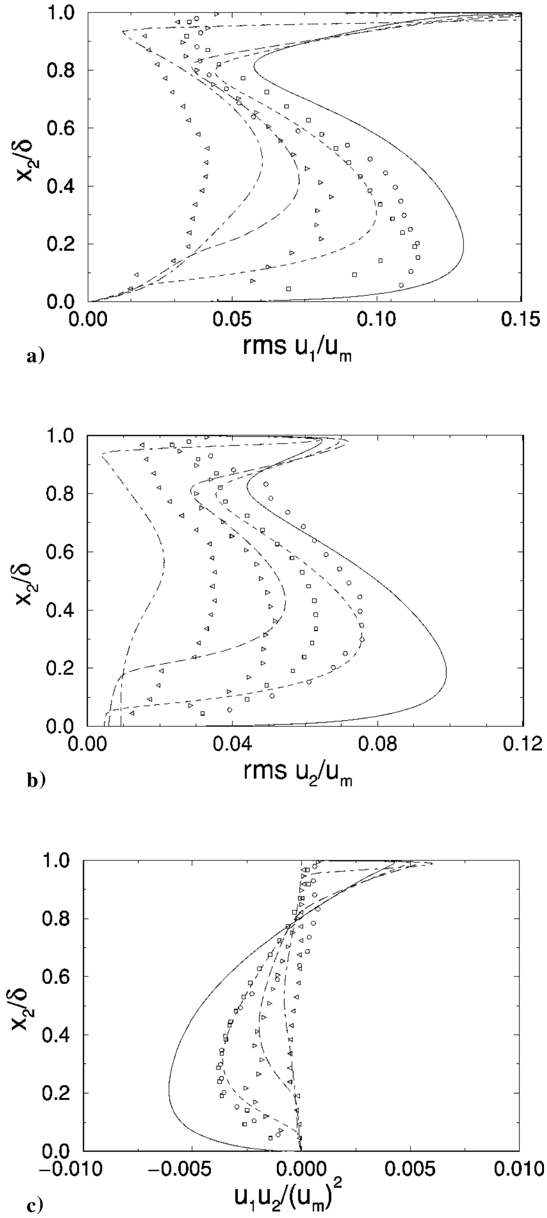

Fig. 13 Turbulent velocity fluctuations normalized by the bulk velocity in different sections: $\sigma_s = 0.2$. a) $(\widetilde{u_1''u_1''})^{1/2}/u_m$; b) $(\widetilde{u_2''u_2''})^{1/2}/u_m$; c) $(\widetilde{u_1''u_2''})/u_m^2$. Symbols: experimental data; lines: RSM simulation. $x_1 = 22$ cm: ◁, –·–; 35 cm: ▷, – – –; 45 cm: □, - - - -; 57 cm: ○, ——.

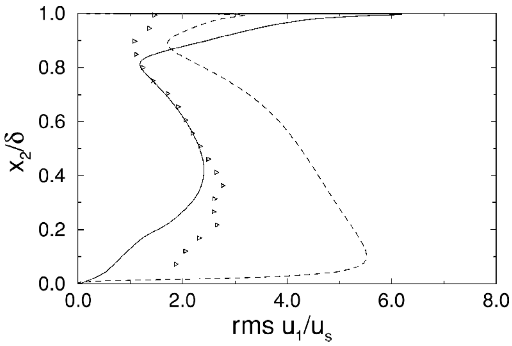

a) $x_1 = 35$ **cm,** ▷

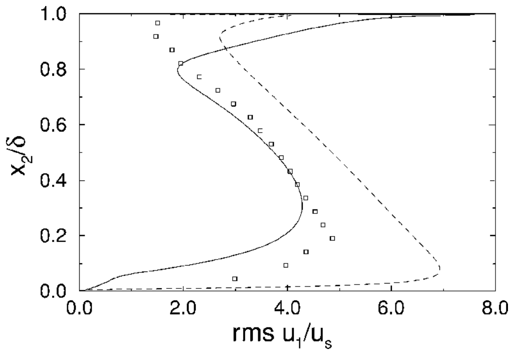

b) 45 cm, □

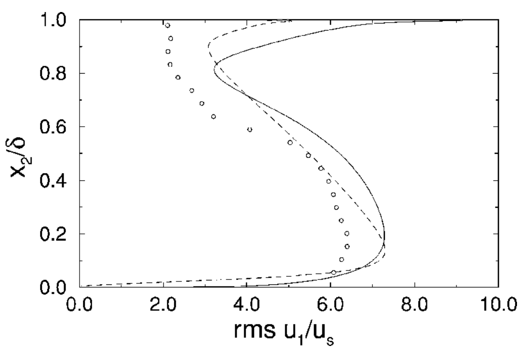

c) 57 cm, ○

Fig. 14 Rms of streamwise velocity fluctuations in different sections nomalized by the injection velocity, a) $(\widetilde{u_1''u_1''})^{1/2}/u_s$. $\sigma_s = 0.2$. **Symbols: experimental data; - - -,** k–ϵ **profiles; ——: RSM profiles.**

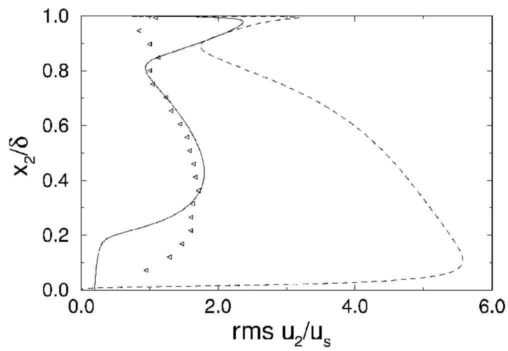

a) $x_1 = 35$ **cm,** ▷

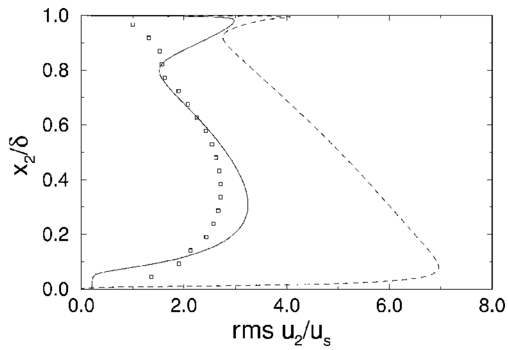

b) 45 cm, □

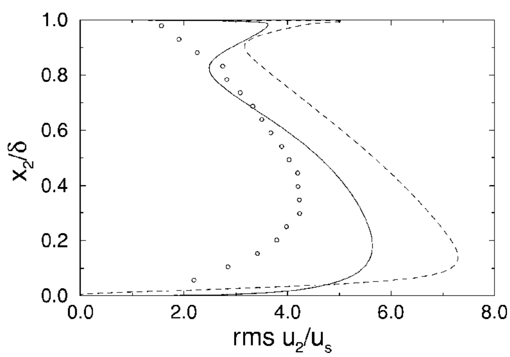

c) 57 cm, ○

Fig. 15 Rms of normal velocity fluctuations in different sections normalized by the injection velocity, a) $(\widetilde{u_2''u_2''})^{1/2}/u_s$. $\sigma_s = 0.2$. **Symbols: experimental data; - - -:** k–ϵ **profiles; ——: RSM profiles.**

the turbulence are well reproduced by the Reynolds-stress model, although some minor discrepancies with the experimental data are observed for the last section. However, the turbulence levels do not agree with the experimental data near the impermeable side ($x_2 = \delta$). This disagreement could be attributed to the measurements that are not accurate in the vicinity of the impermeable wall because the hot-wire probe is introduced through the wall (see Fig. 1). As expected, the intensity of the turbulence velocity fluctuations in the streamwise direction is higher than that in the direction normal to the wall. To illustrate the capability of the Reynolds-stress model in the prediction of the turbulent stresses, numerical simulations have also been performed using the standard k–ϵ model. The model considered in this application incorporates the damping functions of Myong and Kasagi.[38] Figures 14 and 15 show the rms of the streamwise and normal turbulent velocity fluctuations normalized by the injection velocity $(\widetilde{u_1''u_1''})^{1/2}/u_s$, $(\widetilde{u_2''u_2''})^{1/2}/u_s$ in different cross sections of the channel located at $x_1 = 35$, 45, and 57 cm. As already observed, the RSM turbulent model is able to reproduce the evolutions of the Reynolds stresses with good agreement, contrary to the k–ϵ model, which overpredicts the turbulent stresses by about 300% in the first sections.

Conclusions

Predictions of channel flows with fluid injection through a porous wall have been made using an advanced Reynolds-stress model incorporating transport equations of the stress components and the dissipation rate. Comprehensive comparisons with experimental data have been presented. It is found that the Reynolds-stress model is able to reproduce the mean velocity profiles and the transition process. This model has also predicted the turbulent stresses in good agreement with the experimental data, contrary to the standard k–ϵ model. Because of the presence of the impermeable and permeable walls, the development of turbulence has occured at two different locations in the channel. Effects of pseudoturbulence in injected fluid through the porous surface have also been investigated. It has been observed that the turbulence fluctuations introduced in the injected flow can anticipate or delay the second flow transition from laminar to turbulent regime. When the injected turbulence level is greater than a critical threshold, the turbulence intensity in the downstream location of the mean-flow transition is not modified. The present flow prediction has also revealed that the turbulence is developed more rapidly near the impermeable wall in comparison with the permeable wall, even if turbulence fluctuations are introduced in the injected flow.

References

[1]Chaouat, B., "Flow Analysis of a Solid Propellant Rocket Motor with Aft Fins," *Journal of Propulsion and Power*, Vol. 13, No. 2, 1997, pp. 194–196.

[2]Taylor, G., "Fluid Flow in Region Bounded by Porous Surfaces," *Proceedings of the Royal Society of London*, series 234 A, Vol. 1119, 1956, pp. 456–475.

[3]Culick, F. E. C., "Rotational Axisymmetric Mean Flow and Damping of Acoustic Waves in Solid Propellant Rocket Motors," *AIAA Journal*, Vol. 4, No. 8, 1966, pp. 1462–1464.

[4]Yamada, K., Goto, M., and Ishikawa, N., "Simulative Study on the Erosive Burning of Solid Rocket Motors," *AIAA Journal*, Vol. 14, No. 9, 1976, pp. 1170–1176.

[5]Varapaev, V. N., and Yagodkin, V. I., "Flow Stability in a Channel with Porous Walls," *Izvestiya Akademii Nauk SSSR, Mekahanika Zhidkosti i Gaza*, Vol. 4, No. 5, 1969, pp. 91–95.

[6]Casalis, G., Avalon, G., and Pineau, J. P., "Spatial Instability of Planar Channel Flow with Fluid Injection Through Porous Walls," *Physics of Fluid*, Vol. 10, No. 10, 1998, pp. 2558–2568.

[7]Sviridenkov, A. A., and Yagodkin, V. I., "Flows in the Initial Sections of Channels with Permeable Walls," *Fluid Dynamics*, Vol. 11, No. 5, 1976, pp. 43–48.

[8]Beddini, R. A., "Injection-Induced Flows in Porous-Walled Ducts," *AIAA Journal*, Vol. 11, No. 6, 1986, pp. 1766–1773.

[9]Donalson, C. D., "Calculation of Turbulent Shear Flows for Atmospheric and Vortex Motions," *AIAA Journal*, Vol. 10, No. 1, 1972, pp. 4–12.

[10]Dunlap, R., Willoughby, P. G., and Hermsen, R. W., "Flowfield in the Combustion Chamber of a Solid Propellant Rocket Motor," *AIAA Journal*, Vol. 12, No. 10, 1974, pp. 1440–1443.

[11]Sabnis, J. S., Madabhushi, R. K., and McDonald, H., "Navier–Stokes Analysis of Propellant Rocket Motor Internal Flows," *AIAA Journal*, Vol. 5, No. 6, 1989, pp. 657–664.

[12]Sabnis, J. S., Madabhushi, R. K., Gibeling, H. J., and Donald, H. M., "On the Use of k–ϵ Turbulence Model for Computation of Solid Rocket Internal Flows," AIAA Paper 89-2558, July 1989.

[13]Traineau, J. C., Hervat, P., and Kuentzmann, P., "Cold Flow Simulation of a Two-Dimensional Nozzleless Solid Rocket Motor," AIAA Paper 86-1147, June 1986.

[14]Chaouat, B., "Computation Using k–ϵ Model with Turbulent Mass Transfer in the Wall Region," *11th Symposium on Turbulence Shear Flows*, edited by Université Joseph Fourier, Grenoble, France, Vol. 2, 1997, pp. 2.71–2.76.

[15]Liou, T., and Lien, W., "Numerical Simulations of Injection-Driven Flows in a Two-Dimensional Nozzleless Solid-Rocket Motor," *Journal of Propulsion and Power*, Vol. 11, No. 4, 1995, pp. 600–606.

[16]Liou, T., Lien, W., and Hwang, P., "Transition Characteristics of Flowfield in a Simulated Solid-Rocket Motor," *Journal of Propulsion and Power*, Vol. 14, No. 3, 1998, pp. 282–289.

[17]Apte, S., and Yang, V., "Unsteady Flow Evolution in Porous Chamber with Surface Mass Injection, Part 1: Free Oscillation," *AIAA Journal*, Vol. 39, No. 8, 2001, pp. 1577–1586.

[18]Avalon, G., Casalis, G., and Griffond, J., "Flow Instabilities and Acoustic Resonance of Channels with Wall Injection," AIAA Paper 98-3218, July 1998.

[19]Speziale, C. G., Sarkar, S., and Gatski, T. B., "Modelling the Pressure-Strain Correlation of Turbulence: an Invariant Dynamical Systems Approach," *Journal of Fluid Mechanics*, Vol. 227, 1991, pp. 245–272.

[20]Gibson, M. M., and Launder, B. E., "Ground Effects on Pressure Fluctuations in the Atmospheric Boundary Layer," *Journal of Fluid Mechanics*, Vol. 86, 1978, pp. 491–511.

[21]Durbin, P. A., "Separated Flow Computations with the k–ϵ–v^2 Model," *AIAA Journal*, Vol. 33, No. 4, 1995, pp. 659–664.

[22]Parnex, S., Durbin, P. A., and Behnia, M., "Computations of 3-D Turbulent Boundary Layers Using V2F Model," *Flow, Turbulence and Combustion*, Vol. 60, 1998, pp. 19–46.

[23]Durbin, P. A., and Reif, B. A. P., *Statistical Theory and Modeling for Turbulent Flows*, Wiley, New York, 2001, pp. 147–199.

[24]Launder, B. E., and Shima, N., "Second Moment Closure for the Near Wall Sublayer: Development and Application," *AIAA Journal*, Vol. 27, No. 10, 1989, pp. 1319–1325.

[25]Huang, P. G., and Coakley, T. J., *Near-Wall Turbulent Flows*, edited by R. M. C. So, C. G. Speziale, and B. E. Launder, Elsevier, 1993, pp. 199–208.

[26]Chaouat, B., "Simulations of Channel Flows with Effects of Spanwise Rotation or Wall Injection Using a Reynolds Stress Model," *Journal of Fluid Engineering*, Vol. 123, 2001, pp. 2–10.

[27]Favre, A., "Equations des Gaz," *Journal de Mécanique Théorique*, Vol. 4, No. 3, 1963, pp. 362–421.

[28]Chaouat, B., "Modélisation et Simulation des Ecoulements Turbulents dans les Propulseurs à Propergol Solide," Ph.D. Dissertation, Dept. of Mechanics, Univ. of Paris, Oct. 1994.

[29]Shima, N., "Prediction of Turbulent Boundary Layers with a Second-Moment Closure: Part I—Effects of Periodic Presure Gradient, Wall Transpiration and Free-Stream Turbulence. Part II—Effects of Streamline Curvature and Spanwise Rotation," *Journal of Fluid Engineering*, Vol. 115, 1993, pp. 56–69.

[30]Chaouat, B., "Numerical Simulations of Fully Developed Channel Flows Using k–ϵ, Algebraic and Reynolds Stress Models," AIAA Paper 99-0158, Jan. 1999.

[31]Roe, P. L., "Approximate Riemann Solvers, Parameter Vectors and Difference Schemes," *Journal of Computational Physics*, Vol. 43, 1981, pp. 357–372.

[32]Dutoya, D., and Errera, P., "Une Décomposition Formelle du Jacobien des Equations d'Euler. Application à des Schémas Numériques Decentrés," *La Recherche Aérospatiale*, Vol. 1, 1992, pp. 25–35.

[33]Hinze, J. O., "*Turbulence*, McGraw–Hill, New York, 1975, pp. 586–770.

[34]Pimenta, M., and Moffat, R. J., "Stability of Flow Through Porous Plates: Coalescent Jets Effect," *AIAA Journal*, Vol. 12, No. 10, 1974, pp. 1438–1440.

[35]Tong, K., and Knight, C. J., "Flow Around an Isolated Porous Tube with Nonuniform Wall Thickness," *AIAA Journal*, Vol. 17, No. 11, 1979, pp. 1262, 1263.

[36]Ramachandran, N., Heaman, J., and Smith, A., "An Experimental Study of the Fluid Mechanics Associated with Porous Walls," AIAA Paper 92-0769, Jan. 1992.

[37]Huesmann, K., and Eckert, E., "Studies of the Laminar Flow and the Transition to Turbulence in Porous Tubes with Uniform Injection Through the Tube Wall," *Warme und Stoffubertragung*, Vol. 1, 1968, pp. 1–9.

[38]Myong, H., and Kasagi, N., "A New Approach to the Improvement of k–ϵ Turbulence Model for Wall-Bounded Shear Flows," *JSME International Journal*, Vol. 33, No. 1, 1990, pp. 63–72.